Chapter 6
Mesoscale Analysis of Flood Discharge Atomization

6.1 Background

Flood discharge atomization (FDA) refers to a phenomenon in which a flow discharged at a high velocity first spalls in air and entrains a large amount of air and subsequently falls into and splashes the downstream water as a result of an intense impact, resulting in local precipitation in the immediate region and a drift of mist over the far region. FDA is one of the issues that require attention in high-head dam projects. FDA has serious consequences if not treated properly. For example, FDA can damage power plants and trigger riverbank landslides in heavy-precipitation regions. Currently, there are three main approaches for studying FDA: (1) predicting FDA through mechanical analysis and modeling of the motion of water droplets (Hoyt and Taylor 1977; Liang 1992; Sun and Liu 2008); (2) simulating real-world FDA through large-scale model tests (Liu et al. 2005; Wang et al. 2013); and (3) estimating the FDA conditions of planned structures through comparison with the FDA conditions of built structures based on prototype observations (Lian et al. 2014). Apart from the flow conditions (e.g., the flow velocity, flow rate, mode of entry into water, and form in air), FDA is affected by the surrounding terrain, meteorological conditions, and even valley winds. As a result, it is extremely difficult to predict FDA. A combination of various prediction methods is often required to give an approximate prediction of the range and intensity of FDA.

While it is difficult to accurately predict FDA, one thing is certain—the in-depth determination of its intrinsic mechanical mechanism is imperative. Evidently, based on its formation process, FDA is, in essence, a macroscopic assembly of mesoscale phenomena, similar to cavitation erosion and aerated flows, which have been discussed in the previous chapters. Hence, the intrinsic pattern of FDA can be truly understood only by mesoscale analysis.

The FDA problems associated with a group of arch dams over 200 m in height in China are highly representative (Sun 2009). These dams are characterized by large heights, high flow rates, and narrow river valleys. As a result, intense FDA directly affects the slope stability of the banks behind these dams. The Ertan hydropower

W. Xu, *Mesoscale Analysis of Hydraulics*,
https://doi.org/10.1007/978-981-15-9785-5_6

station on the Yalong River discharges floods through the simultaneous use of two rows of dam outlets and collision of flows in air, pioneering flood discharge at a high flow rate by high arch dams. In addition, owing to its large height, high flow rate, and pronounced FDA problem, the Ertan hydropower station is a milestone in FDA research. A series of high arch dams subsequently constructed, including the Xiaowan hydropower station on the Lancang River, the Xiluodu hydropower station on the Jinsha River, and the Baihetan hydropower station, all drew lessons from the way the Ertan hydropower station discharges floods. However, when the Jinping-I hydropower station on the Yalong River was later designed, the necessity and feasibility of the simultaneous use of two rows of dam outlets without collisions of flows in air garnered attention due to the geological conditions of the downstream slopes. Thus, it is necessary to determine the increase in the extent of FDA resulting from collisions of flows in air, which requires an understanding of the mesoscale mechanism of FDA caused by collisions of flows in air.

In fact, not only is research on the mesoscale mechanism of FDA caused by collisions of flows in air insufficient, but mesoscale research on the splashing of water caused by impacting flows as well as spallation of flows in air is also deficient. These issues are discussed in this chapter.

6.2 Jet Spallation in Air

There are three main causes of FDA, namely, jet spallation in air, jet collision, and water splash by plunging jets (Reitz and Bracco 1982; Lian et al. 2006; Choo and Kang 2007). Figure 6.1 shows the spallation of a jet in air. After leaving the exit of the nozzle, the jet was able to remain relatively stable within a short distance. After traveling a certain distance, the jet began to become unstable. As the distance increased, the jet became increasingly unstable, and water droplets and water-droplet masses began to break away from the surface of the flow.

Figure 6.2 shows generalized diagrams of several main modes of the formation of water droplets during the spallation process. Overall, there are three scenarios for the formation of water droplets. (1) A low-velocity jet has a turbulent surface, and consequently, a small finger-shaped water column is formed on its surface. The difference between the velocities of the water column and the mainstream of the jet becomes increasingly significant under the action of air. After reaching a certain length, the water column contracts to form a nearly spherical water droplet as a result of its surface tension. However, the water droplet is still linked to the jet via a "ligament". Ultimately, the finger-shaped water column breaks up into several water droplets that are directly separated from the mainstream of the jet. Due to air drag, the water droplets continue to deform and vibrate. At this time point, the water droplets are relatively large and vary relatively insignificantly in diameter. The spallation angle of each water droplet is relatively small (Fig. 6.3). (2) The mainstream of a high-velocity jet is extremely unstable. As a result, the jet breaks up into sheet- and thin membrane-like water structures. Due to the high velocity, the water structures

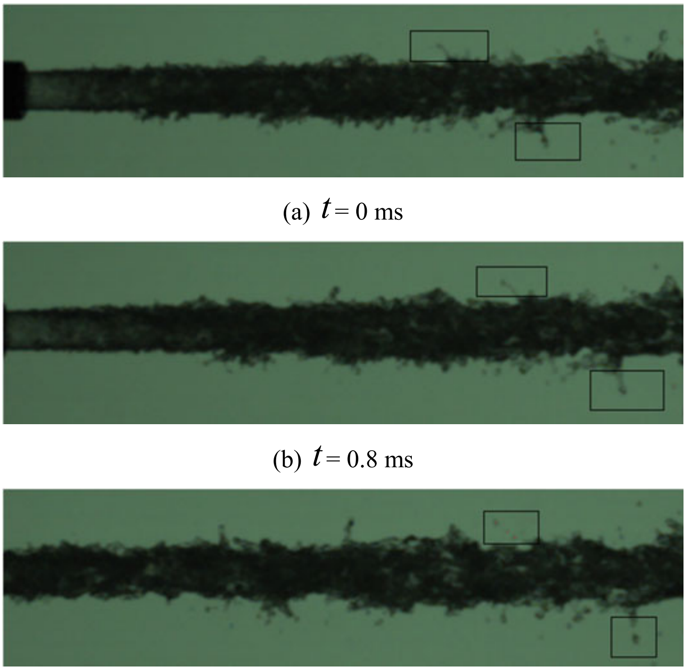

(a) $t = 0$ ms

(b) $t = 0.8$ ms

(c) $t = 2.3$ ms

Fig. 6.1 Separation of the water droplets from a jet (nozzle diameter D = 5.5 mm, pressure P = 0.3 MPa, flow velocity v = 16.32 m/s, Reynolds number Re = 89,815, and Weber number We = 20,953)

formed from the breaking up of the jet further break up into water droplets of varying sizes as well as fine mist droplets. These droplets have large spallation angles and affect a relatively large space. (3) A water droplet formed from the spallation of a jet is relatively large in size and moves at a relatively high velocity. As a result, its surface tension is insufficient for maintaining its form in the air. Consequently, the water droplet breaks up into finer water and mist droplets (Fig. 6.4). Moreover, water droplets are formed from collisions between the water droplets formed from the spallation of a jet, i.e., collisions between high-velocity water droplets lead to the formation of water and mist droplets of smaller sizes. However, this is not a main cause of the formation of water droplets based on the captured images.

6.2.1 Velocity Distribution of Jet-Spalled Water Droplets

To quantitatively study the jet spallation characteristics, the motion characteristics of a large number of water droplets spalled from jet mainstreams were statistically

(a) Main mode of the formation of water droplets from a low-velocity jet

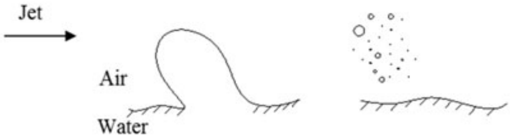

(b) Main mode of the formation of water droplets from a high-velocity jet

(c) Breaking up of a water droplet

Fig. 6.2 Generalized diagrams depicting several main modes of formation of water droplets

analyzed. Because the axial velocity v_X of a water droplet was significantly higher than its vertical velocity v_Y, the resultant velocity v_r calculated using an equation differed insignificantly from v_X. In addition, the statistical probability distribution of v_r was highly similar to that of v_X, as shown in Fig. 6.5. In each histogram in Fig. 6.5, the bar width represents a velocity range of 0.25 m/s. In addition, each velocity v' on the x-axis represents a velocity range from $(v' - 0.25)$ to v' m/s, and the bar height represents the velocity value within this velocity range. The probability distributions of the v_X and v_r of the water droplets spalled from a low-velocity jet each approximately exhibited a bell-shaped pattern, i.e., a relatively small number of values were distributed at the two ends, while a relatively large number of values were distributed in the center. However, as the cross-sectional mean velocity of the jet increased to a relatively large value, each distribution gradually changed from a notable bell-shaped pattern to a flat pattern. The x-axis shows that the velocity distribution range gradually increased as the cross-sectional mean velocity of the jet increased. This suggests that as the cross-sectional mean velocity of jet increased, there was an increase in the distribution ranges of v_X and v_r and a decrease in the probability of each single velocity. This indicates that the water-droplet spallation velocity distribution is more uniform at a high flow velocity.

To more accurately describe the statistical probability distributions of the droplet velocity and to test the overall normality, the p-value of the normality test for the data was calculated using the W-test method. The following criterion was used: If the p-value is greater than 0.05, the hypothesis that the data are normally distributed is not rejected. The closer the p-value is to 1, the more the data conform to a normal

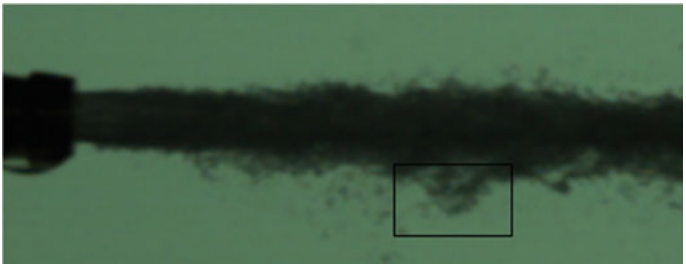

(a) $t = 0$ ms

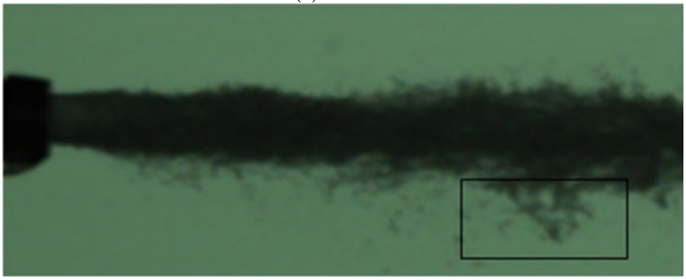

(b) $t = 0.48$ ms

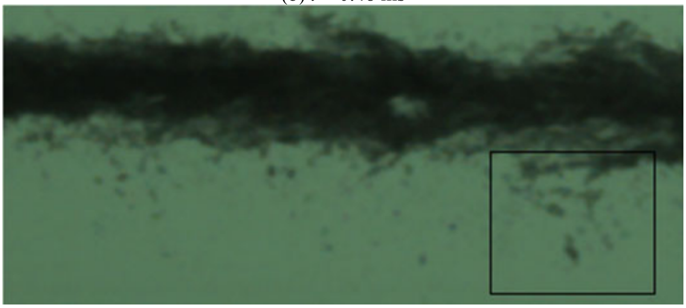

(c) $t = 1.95$ ms

Fig. 6.3 Spallation of a high-velocity jet ($D = 4.5$ mm, $P = 0.5$ MPa, and $v_0 = 21.49$ m/s)

distribution. Table 6.1 summarizes the calculation results. The kurtosis κ is primarily used to measure the thickness of the tails of a distribution graph and can reflect the leptokurtosis of the top of a distribution graph and the thickness of the tails at its two ends. However, κ is unrelated to the value of the top of a distribution graph. The κ of each univariate normal distribution is 3 and is unrelated to its mean and standard deviation. κ is calculated using Eq. (6.1). A $\kappa > 3$ suggests that the peak of the distribution graph is relatively steep. A $\kappa < 3$ suggests that the peak of the distribution graph is relatively flat.

$$\kappa = \frac{E(X - \mu)^4}{\sigma^4} \tag{6.1}$$

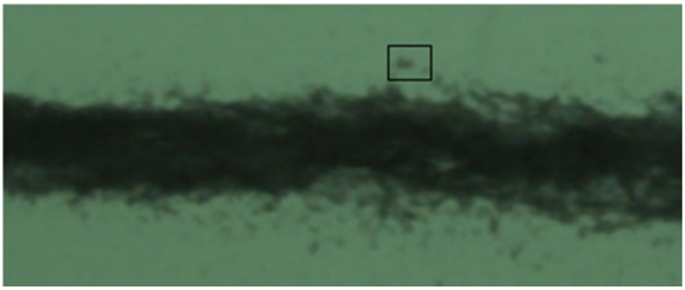

(a) $t = 0$ ms

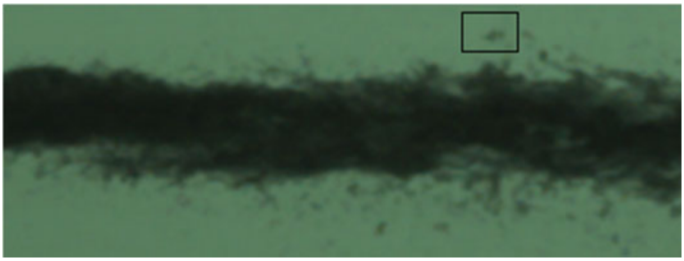

(b) $t = 0.3$ ms

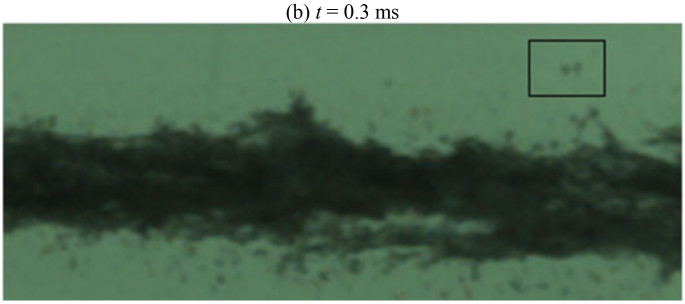

(c) $t = 2.1$ ms

Fig. 6.4 Spallation of a high-velocity jet ($D = 4.5$ mm, $P = 0.6$ MPa, and $v_0 = 22.74$ m/s)

The skewness s reflects the symmetry of a distribution graph and is calculated using the following equation:

$$s = \frac{E(X - \mu)^3}{\sigma^3} \tag{6.2}$$

where σ and μ are the standard deviation and mean of the samples. The variations in the μ and σ of the resultant velocity v_r values show the variation in the shape of the normal distribution corresponding to μ and σ. Then, based on s and κ, the difference from a normal distribution can be determined. As demonstrated in Table 6.1, as σ increased, there was a gradual decrease in the peak extreme value $\left(\sqrt{2\pi}\sigma\right)^{-1}$, a gradual increase in the flatness of the shape of the normal distribution, and an

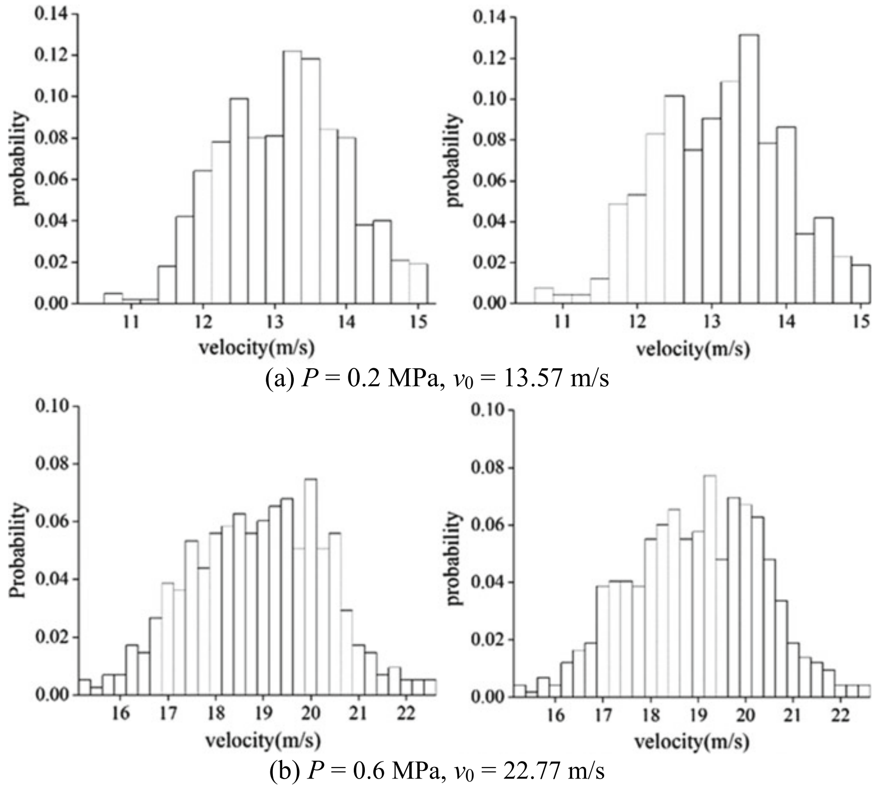

Fig. 6.5 Probability distributions of the axial velocity v_X (left) and resultant velocity v_r (right) at various jet velocities v_0 with a nozzle diameter D of 5.5 mm

increase in the degree of dispersion. In addition, an increase in μ caused the normal distribution to gradually shift to the right. However, as μ increased beyond a certain value, the normal distribution began to shift at a decreasing rate. At a low flow velocity, σ was smaller and the data were more concentrated for the jet discharged from the nozzle with a diameter D of 4.5 mm (hereinafter the 4.5-mm jet) than the jet discharged from the nozzle of $D = 5.5$ mm (hereinafter the 5.5-mm jet). As the pressure P increased to 0.5 MPa, the 4.5-mm jet dispersed to a much more significant extent than the 5.5-mm jet. In addition, the normally distributed data for the 4.5-mm jet were much more dispersed and the shape of their normal distribution was flatter than those of the 5.5-mm jet.

Next, the effects of κ and s on the shape of the distribution graph were taken into consideration. When $P = 0.2$ MPa, κ was positive for the 4.5-mm jet and negative for the 5.5-mm jet. This suggests that the peak of the graph for the 4.5-mm jet was steeper than that for the 5.5-mm jet. In addition, s was negative for the 4.5-mm jet and positive for the 5.5-mm jet (the difference was insignificant). This indicates that the data for the 5.5-mm jet were basically symmetrical, whereas the data for the

Table 6.1 Distribution characteristics of the axial velocity v_X and resultant velocity v_r

Working conditions	D (mm)	v_X					v_r				
		s	κ	σ	μ	p-value	s	κ	σ	μ	p-value
1	4.5	–	–	–	–	–	–	–	–	–	–
2		−0.753	0.674	0.776	13.38	0	−0.758	0.703	0.774	13.38	0
3		−0.144	0.254	0.735	16.02	0.294	−0.143	0.219	0.732	16.03	0.344
4		−0.195	0.536	1.399	18.31	0.019	−0.176	0.575	1.365	18.35	0.024
5		−0.694	0.473	2.576	18.3	0	−0.687	0.488	2.553	18.39	0
6		−0.423	−0.466	3.081	18.51	0	−0.432	−0.458	3.052	18.64	0
7	5.5	–	–	–	–	–	–	–	–	–	–
8		−0.062	−0.368	0.860	12.99	0.215	0.061	−0.369	0.856	13.00	0.244
9		−0.264	0.225	0.990	14.77	0.137	−0.262	0.223	0.987	14.79	0.152
10		−0.181	−0.130	1.108	15.82	0.322	−0.186	−0.114	1.101	15.85	0.351
11		−0.171	−0.339	1.282	16.87	0.143	−0.171	−0.317	1.275	16.92	0.179
12		−0.076	−0.399	1.972	18.76	0.170	−0.093	−0.374	1.950	18.83	0.171

4.5-mm jet were left-skewed and their distribution had a long tail pointing to the left. This is consistent with the distribution graph. When $P = 0.3$ MPa, similar graphs were observed, but the graph for the 4.5-mm jet had a higher peak and thicker tails than those for the 5.5-mm jet. The s values of the graphs differed insignificantly and were both very small. When $P = 0.6$ MPa, the σ of the 4.5-mm jet was much larger. However, the κ values of both graphs were negative and differed insignificantly. This suggests that the distribution of the v data for the 4.5-mm jet was much more dispersed but slightly left-skewed.

When $D = 5.5$ mm, κ was lower than that of the normal distribution corresponding to the μ and σ in most cases, though the difference was insignificant. This suggests a slightly flatter peak (i.e., thinner tails) than a normal distribution and a relatively low probability of extreme values. The graphs were left-skewed, albeit insignificantly, as shown in the figure. The data for the 4.5-mm jets were similar to those for the 5.5-mm jets in terms of the distribution shape. The distribution graphs for the 4.5-mm jets were all left-skewed, albeit insignificantly. In addition, the peaks of the distributions for the 4.5-mm jets were steeper, albeit insignificantly, than that of a normal distribution.

The normality test results for the v data show the following. When $D = 5.5$ mm, the significance was greater than 0.05, and the distribution of v_X conformed to the normality assumption. The normality test results for the 4.5-mm jets show that the data for the 4.5-mm jet with a flow velocity of 16.32 m/s conformed to a normal distribution. However, the resultant velocity data for the 4.5-mm jets did not conform to a normal distribution, except for those for the 4.5-mm jet with a velocity of 19.27 m/s, which were relatively weakly normally distributed. When $D = 4.5$ mm, water droplets began to be spalled at a velocity of 13.41 m/s but at a very small quantity. The limited statistical data samples failed the normality test. Intense spallation began as the velocity increased to 19.27 m/s. However, the statistical data samples for mist droplets at this high velocity also failed the normality test. The spallation intensity of the 5.5-mm jets under the conditions selected for statistical analysis was between that of the 4.5-mm jet with the minimum velocity and that of the 4.5-mm jet with the maximum velocity. Thus, the normality of the droplet velocity was related to the spallation intensity.

Based on the distribution graph parameters and normality test results for the 4.5- and 5.5-mm jets, the resultant velocity data for low jet flow velocity ($P = 0.2$ and 0.3 MPa) 4.5-mm jets were distributed in a more concentrated pattern than those for the 5.5-mm jets. At high jet flow velocity ($P = 0.5$ and 0.6 MPa), the data for the 4.5-mm jets were more dispersed and distributed in a more scattered pattern. All the graphs were left-skewed, albeit insignificantly, and were basically symmetrical. At a constant D, as the jet flow velocity increased, there was a gradual increase in the extent of the dispersion of the droplet velocity. Thus, the variation in the distribution curve of the droplet velocity with the jet flow velocity can be summarized as follows: as the jet flow velocity increased, the bell-shaped curve shifted to the right (as the jet flow velocity increased beyond a certain value, there was a decrease in the rate of the shift of the mean value) and gradually became flat. The experimental results obtained in this study show that the normality of the distribution of the droplet velocity was related to the spallation intensity.

Figures 6.6 and 6.7 show the cumulative probability curves of v_r when $D = 5.5$ and 4.5 mm, respectively. An "S" shape can be observed in each distribution curve. Thus, examining the cumulative probability distribution can more directly help determine the rate and range of change in v_r. A rightward shift can be observed in the distribution of v_r with an increasing jet flow velocity when $D = 5.5$ mm. In addition, a decrease in the slope of the curve can be observed due to an increase in the range of v_r. A similar pattern can be observed in the distribution of v_r when $D = 4.5$ mm—a gradual rightward shift in the distribution curve and a decrease in its slope with an increasing jet flow velocity. Moreover, the v_r curves for the 4.5-mm jet with a high flow velocity intersect at the v_r value of 18 m/s and near the probability of 0.375. This suggests the same probability of water droplets at v_r below 18 m/s.

Table 6.2 summarizes the characteristic droplet velocities of statistical samples at various jet flow velocities. The measured cross-sectional mean flow velocity of

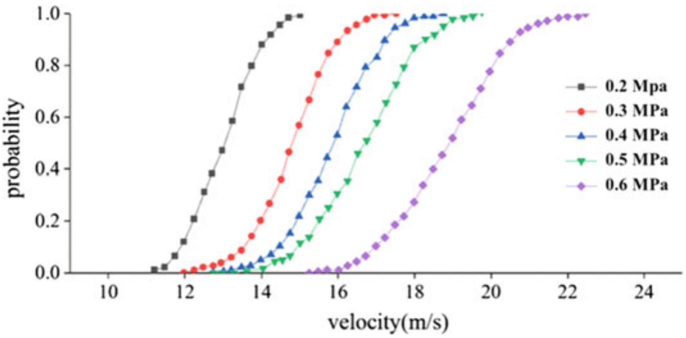

Fig. 6.6 Cumulative probability curves of resultant velocity of water droplets spalled from 5.5-mm jets

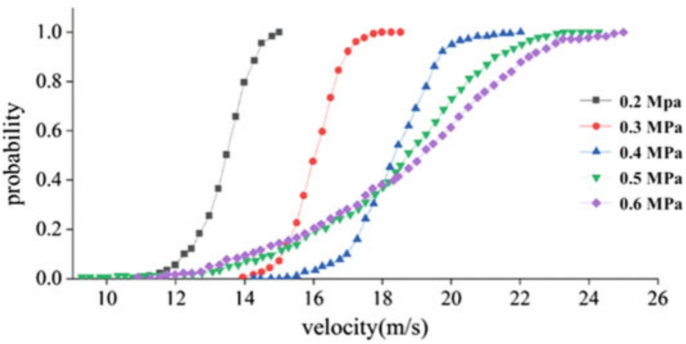

Fig. 6.7 Cumulative probability curves of the v_r of water droplets spalled from 4.5-mm jets

Table 6.2 Characteristic values of the axial velocity v_X and resultant velocity v_r of the water droplets determined from the statistical samples

Jet flow velocity v_0 ($D = 4.5$ mm) (m/s)	v_X (m/s)			v_r (m/s)		
	Max	Min	Average	Max	Min	Average
13.41	14.94	10.71	13.38	14.95	10.71	13.38
16.30	18.42	13.92	16.02	18.43	13.92	16.03
19.05	21.94	14.02	18.31	21.96	14.03	18.35
20.60	23.97	8.93	18.3	24.08	9.13	18.39
22.74	24.91	10.81	18.51	24.97	10.95	18.64
v_0 ($D = 5.5$ mm) (m/s)	v_X (m/s)			v_r (m/s)		
	Max	Min	Average	Max	Min	Average
13.57	14.92	10.53	12.99	14.93	10.54	13
16.32	17.47	11.57	14.77	17.5	11.6	14.79
19.27	18.71	12.66	15.82	18.72	12.67	15.85
21.49	19.469	12.79	16.87	20	12.83	16.92
22.77	22.42	15.05	18.76	22.45	15.08	18.83

each jet was higher than the mean droplet velocity. The turbulence intensity of high-velocity jets was as high as 0.25. A scenario where the cross-sectional mean flow velocity of the jet was lower than the maximum velocity of water droplets was observed in the statistical samples. Figure 6.8 shows the statistical variations in v_X and v_r with the jet flow velocity when $D = 5.5$ mm. As demonstrated in Fig. 6.8, as jet flow velocity increased, both v_X and v_r increased, though nonlinearly.

Figure 6.9 compares the mean v_r values of all the atomized water droplets at various jet flow velocities when $D = 4.5$ and 5.5 mm. As demonstrated in Fig. 6.9, there was an insignificant difference in the mean v_X and v_r of the atomized water

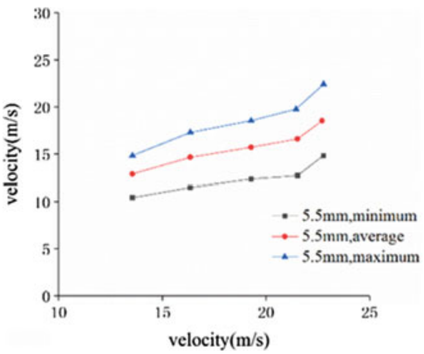

(a) v_X

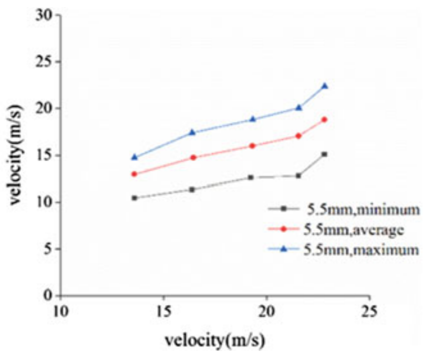

(b) v_r

Fig. 6.8 Variations in the characteristic values of the motion parameters of the spalled water droplets with the cross-sectional mean jet flow velocity v_0 when $D = 5.5$ mm

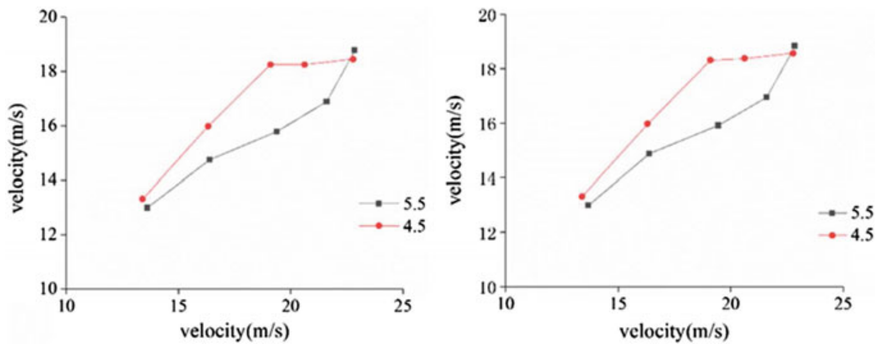

(a) Mean v_X (b) Mean v_r

Fig. 6.9 Comparison of the mean values of the motion parameters of the spalled water droplets at various D values and jet flow velocities

droplets between the 4.5- and 5.5-mm jets at a low jet flow velocity ($P = 0.2$ MPa). As jet flow velocity increased, there was an increase in the differences in the mean v_X and v_r between the two jet sizes. The difference reached the maximum when $P = 0.4$ MPa and gradually decreased as P increased beyond 0.4 MPa. When $P =$ 0.6 MPa, the mean v_X and v_r of the water droplets atomized from the 5.5-mm jet were almost the same as those of the water droplets atomized from the 4.5-mm jet.

6.2.2 Distribution of the Moving Directions of the Water Droplets Formed by Jet Spallation

In this section, the distributions of the vertical velocity v_Y and spallation angle α_s are examined. The v_Y of the water droplets spalled from a low-velocity jet was very low, and they moved almost in parallel to the mainstream of the jet. As a result, most of the water droplets moved at a low v_Y (Fig. 6.10). As v_Y increased, there was a gradual decrease in the number of water droplets. A descending sloped shape at a certain angle can be observed in the probability distribution of v_Y. As the jet flow velocity increased, there was a gradual increase in the number of water droplets formed from jet spallation. Under this condition, v_Y was distributed in an asymmetrical bell-shaped pattern. As the jet flow velocity increased, there was a corresponding increase in the maximum v_Y and the maximum α_s. In addition, a gradual rightward shift in the v_Y and α_s corresponding to the respective highest probabilities as well as a gradual decrease in the extreme values of v_Y and α_s corresponding to the respective highest probabilities can be observed in the distribution graphs with increasing jet flow velocity. This suggests that as the mean α_s of the water droplets increased, the distribution of the numbers of water droplets of various α_s values became increasingly uniform.

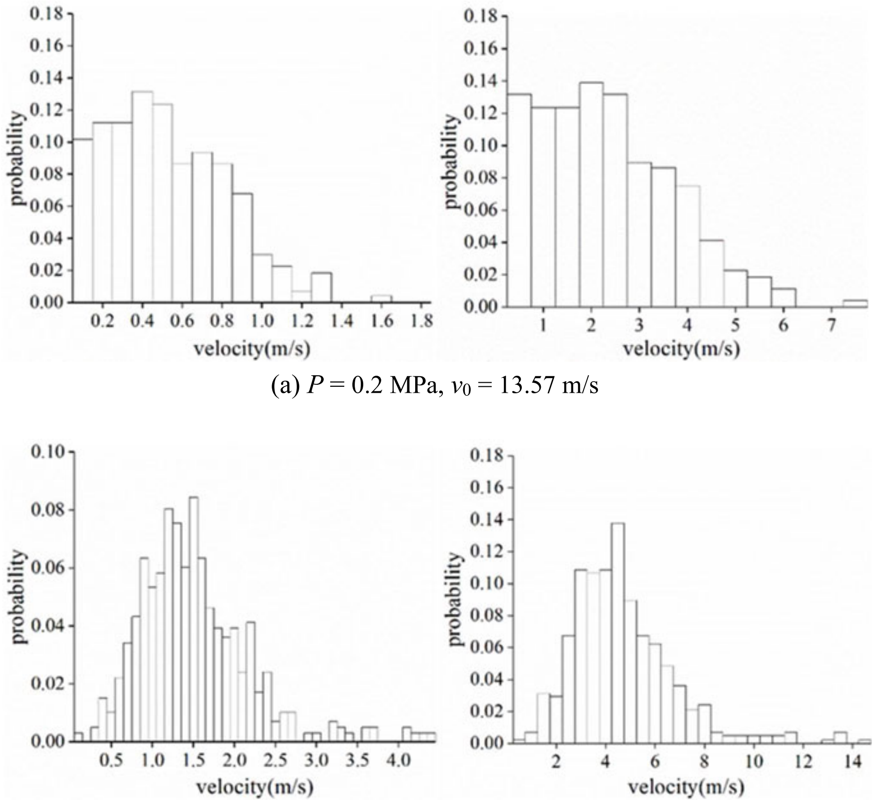

(a) $P = 0.2$ MPa, $v_0 = 13.57$ m/s

(b) $P = 0.6$ MPa, $v_0 = 22.77$ m/s

Fig. 6.10 Probability distributions of the vertical velocity v_Y and spallation angle α_s of the water droplets spalled from 5.5-mm jets at various flow velocities v_0 (the bar width represents a range of 0.1 m/s in the v_Y distribution graphs and a range of 0.5° in the α_s distribution graphs)

Table 6.3 summarizes the shape characteristics of the probability distribution of the α_s of water droplets. When D remained unchanged ($D = 4.5$ and 5.5 mm), as the jet flow velocity gradually increased, there was a gradual increase in the σ and μ of the α_s values. This suggests that the normal distribution corresponding to σ and μ became gentler, the data became more dispersed, and the axis of symmetry moved to the right as the jet flow velocity increased. At a low jet flow velocity, the normally distributed data corresponding to $D = 4.5$ mm were more concentrated. At a relatively high jet flow velocity, the normally distributed data corresponding to $D = 4.5$ were more dispersed. Next, the kurtosis κ and skewness s of the samples were considered, and the differences between the actual distribution graphs and a normal distribution were analyzed. At a constant D, the s of the distribution of α_s values was positive, regardless of the jet flow velocity. This suggests that the distribution of the α_s values at each jet flow

Table 6.3 Distribution shape characteristics of the vertical velocity v_Y and spallation angle α_s

Jet flow velocity v_0 (m/s)	D (mm)	v_Y					α_s				
		s	κ	σ	μ	p-value	s	κ	σ	μ	p-value
13.41	4.5	1.122	1.430	0.262	0.35	0	1.208	1.705	1.168	1.50	0
16.30		1.120	2.042	0.318	0.45	0	1.209	2.443	1.145	1.61	0
19.05		0.747	0.263	0.607	1.06	0	0.917	0.842	2.007	3.37	0
20.60		0.442	0.239	0.868	1.60	0	0.449	0.027	2.948	5.19	0
22.74		1.110	3.288	1.067	1.80	0	0.645	0.862	3.517	5.82	0
13.57	5.5	0.601	0.034	0.302	0.47	0	0.643	0.075	1.390	2.10	0
16.32		0.821	0.996	0.357	0.72	0	0.808	0.906	1.424	2.82	0
19.27		0.811	0.294	0.446	0.89	0	0.881	0.571	1.685	3.24	0
21.49		1.121	2.520	0.573	1.23	0	1.133	2.263	2.009	4.21	0
22.77		1.246	2.693	0.679	1.46	0	1.403	3.378	2.135	4.47	0

velocity was skewed right, that most of the data were to the left of the mean value, and that the left end of the distribution was relatively thick. The right end of the distribution of the α_s values at each jet flow velocity had a long tail and a positive κ value. This suggests that the peak of the distribution was steeper than that of a normal distribution. At a low jet flow velocity, a higher κ and a smaller σ were found when $D = 4.5$ mm. This suggests that the top of the distribution of the α values was steeper and the data near the top of the distribution were more concentrated when $D = 4.5$ mm. At a relatively high jet flow velocity, a lower κ and a larger σ were found when $D = 4.5$ mm. This suggests that the top of the graph was gentler and the data were more dispersed when $D = 4.5$ mm than when $D = 5.5$ mm. In addition, as demonstrated in Table 6.3, the α_s values at each jet flow velocity exhibited a positive s and were concentrated on the left side (i.e., the low-value side) of the distribution, which had a tail on its right side. The data were subjected to a normality test. As demonstrated in Table 6.3, the significance was 0 when $D = 4.5$ and 5.5 mm. This indicates that the distributions of the α_s values did not conform to the normality assumption.

Hence, the statistical distribution graphs of the α_s values were skewed right, and large extreme values of α_s existed at the same jet flow velocity, albeit in small quantities. As the jet flow velocity increased, the distribution graph of the statistical samples gradually became gentler, and the data became more dispersed. In regard to the distribution of the α_s values at various D values, at a low jet flow velocity, the distribution graph was steeper and the data were more concentrated at a smaller D; at a high jet flow velocity, the α_s values of the water droplets formed from the spallation of a jet discharged from a nozzle with a smaller D were more dispersed.

The distribution graphs of the α_s values observed in the experiment were notably skewed right. This suggests a very low probability of relatively large α_s values in the statistical samples. This is because a relatively large α_s often resulted from a relatively

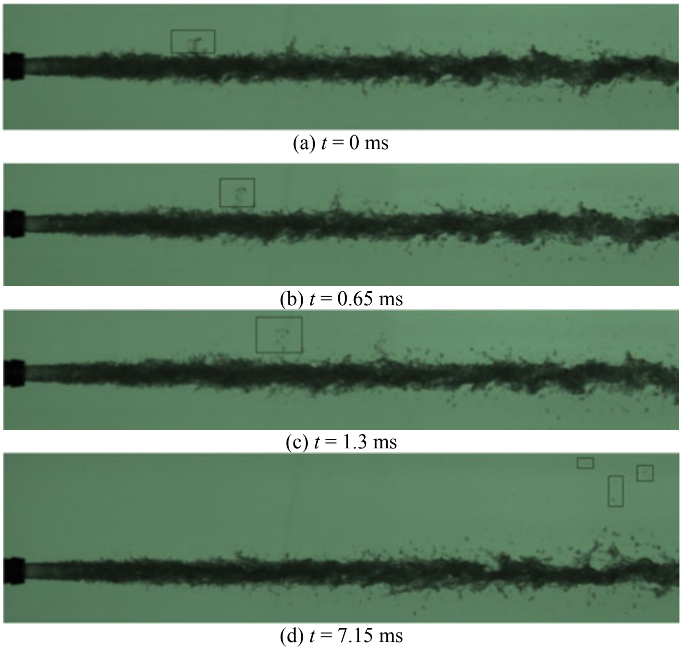

Fig. 6.11 Formation of water droplets from jet dispersion at large α_s values ($D = 5.5$ mm, $P = 0.5$ MPa, and $v_0 = 21.49$ m/s)

significant disturbance of the jet form (as shown in Fig. 6.11). Consequently, there were only a relatively small number of large α values, which exerted an insignificant impact on the formation of water droplets from jet spallation. Thus, the cumulative probability distribution of α_s in the statistical samples could cover the majority of α_s values. Figures 6.12 and 6.13 show the cumulative probability distribution patterns.

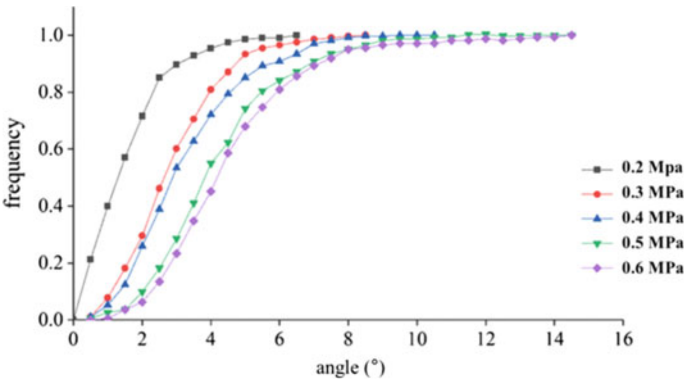

Fig. 6.12 Cumulative probability curves of the α_s of the water droplets spalled from 5.5-mm jets

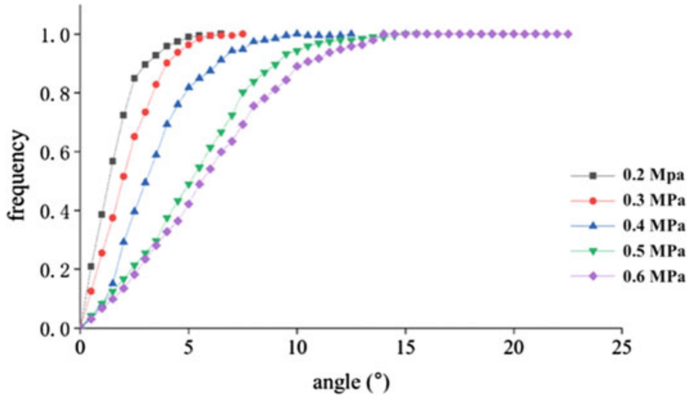

Fig. 6.13 Cumulative probability curves of the α_s of the water droplets spalled from 4.5-mm jets

As demonstrated in Figs. 6.12 and 6.13, α_s increased as the jet flow velocity increased. As the jet flow velocity increased beyond a certain large value, the maximum α_s continued to increase but varied insignificantly. The α_s values of the majority of the water droplets formed from the spallation of 4.5- and 5.5-mm jets at various jet flow velocities were below 14°.

Table 6.4 summarizes the characteristic values of the vertical velocity v_Y and spallation angle α_s of the experimental water-droplet samples formed from jet spallation. As the jet flow velocity increased, there was an increase in the characteristic values of v_Y and α_s. At a constant D, as the jet flow velocity increased, compared to the

Table 6.4 Characteristic values of the vertical velocity v_Y and spallation angle α_s of the water-droplet samples

Jet flow velocity v_0 ($D = 4.5$) (m/s)	v_Y (m/s)			α_s (°)		
	Max	Min	Average	Max	Min	Average
13.41	1.39	0.01	0.35	6.18	0.04	1.5
16.3	1.94	0.01	0.45	7.4	0.03	1.61
19.05	3.36	0.02	1.06	12.21	0.04	3.37
20.6	4.75	0.04	1.6	15.33	0.12	5.19
22.74	8.04	0.01	1.8	22.33	0.02	5.82
v_0 ($D = 5.5$) (m/s)	v_Y (m/s)			α_s (°)		
	Max	Min	Average	Max	Min	Average
13.57	1.55	0.02	0.47	7.3	0.06	2.1
16.32	2.2	0.04	0.72	8.26	0.13	2.82
19.27	2.41	0.07	0.89	10.25	0.24	3.24
21.49	4.23	0.06	1.23	14.24	0.22	4.21
22.77	4.31	0.01	1.46	14.32	0.02	4.47

significant increase in the maximum v_Y and α_s, the mean v_Y and α_s increased, albeit to an insignificant extent, as shown in Figs. 6.14 and 6.15. In addition, the mean v_Y and α_s were much smaller than the maximum v_Y and α_s, respectively. This is consistent with the distribution graphs of v_Y and α_s. Compared to that of a 5.5-mm jet, the maximum α_s of the water droplets formed from the spallation of a 4.5-mm jet increased faster and reached as high as 22.33° (compared to the 14.32° for the water droplets formed from a 5.5-mm jet). The maximum α_s of the water droplets formed from the spallation of a 5.5-mm jet increased more slowly as the jet flow velocity increased than that of a 4.5-mm jet. A comparison of the mean v_Y and α_s of the water droplets formed from the spallation of jets of various sizes found that at a relatively low jet flow velocity, the mean v_Y and α_s of the water droplets decreased as the size of the jet increased.

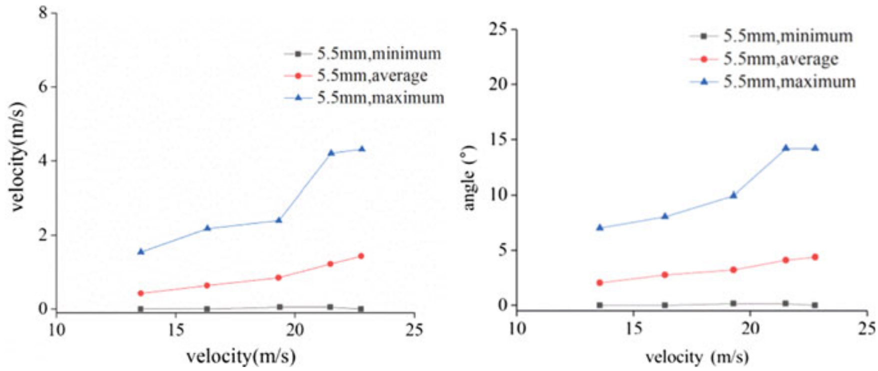

(a) v_Y (b) α_s

Fig. 6.14 Variations in the characteristic values of the spallation angle α_s of water droplets with the cross-sectional mean flow velocity when $D = 5.5$ mm

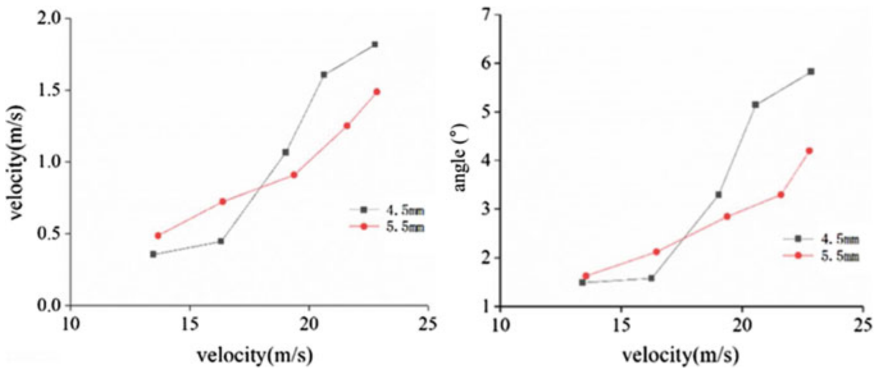

(a) Comparison of the mean v_Y (b) Comparison of the mean α_s

Fig. 6.15 Comparison of the mean values of the motion parameters of water droplets at various nozzle diameters and flow velocities

6.3 Jet Collision in Air

Both physical model tests and theoretical analyses have demonstrated that the distributions of the intensity of the rainfall atomized from two jets when they collide in air and when they do not collide in air differ significantly and that the impingement angle and flow-rate ratio of the two jets significantly affect the distribution of the intensity of the rainfall formed from their spallation after the collision in air (Yuan et al. 2018). Studying the effects of collision on the spallation trajectories of jets as well as the distributions of the characteristic values of several parameters (size, velocity, and quantity) of water droplets during the collision and spallation processes of jets from a mesoscale perspective can facilitate an in-depth understanding of the FDA pattern when jets collide in air.

6.3.1 Characteristics of the Water Droplets Formed by a Jet Collision in Air

In this section, the modes of spallation of two jets after their collision in air are investigated. Collision in air alters the initial form and motion characteristics of jets. The spallation intensity of the nappe formed after a collision in air between two jets is higher than that of the jets. The transverse and streamwise spreading ranges of the postcollision nappe increase as the spatial distance increases (Sanjay and Das 2017a, b). In addition, large numbers of water droplets and water-droplet masses break away from the postcollision nappe at its edges. The number n of water droplets per unit time (i.e., the number frequency of water droplets) is used to measure the number of water droplets at a measuring point:

$$n = \frac{N}{T} \tag{6.3}$$

where N is the number of water droplets collected within the collection time T. Let d be the measured diameter of a water droplet. The probability of a certain diameter d at a measuring point is the ratio of the number n_d of water droplets with a diameter d to N:

$$p_d = \frac{n_d}{N} \tag{6.4}$$

where n_d is the number of water droplets with a certain diameter d. Let v be the velocity of a water droplet. The probability of a certain v is the ratio of the number of water droplets with a velocity v (n_v) to N:

$$p_v = \frac{n_v}{N} \tag{6.5}$$

Let $\overline{v}$ and $\overline{d}$ be the mean velocity and mean diameter of the water droplets at each measuring point, respectively.

Figure 6.16 shows the distribution patterns of n in various streamwise cross-sections at various impingement angle β and flow-rate ratio f values (z is the distance between the location of a vertical cross-section from the collision point between the two jets). In each case, n first increased and then decreased along the streamwise direction and had an extreme value $n_{\max}$. In addition, f had a more significant impact on n than β. According to the theorem of momentum, after the collision, the majority of the water droplets had a velocity component along the streamwise direction, while their vertical and transverse velocity values were random. In the transverse cross-section with the maximum rainfall intensity $I_{\max}$, n decreased along the transverse direction and first decreased and then became stable along the vertical direction (Fig. 6.17).

In the transverse cross-section with $I_{\max}$, $\overline{d}$ first increased and then basically remained stable along the vertical direction. However, overall, as z increased, there

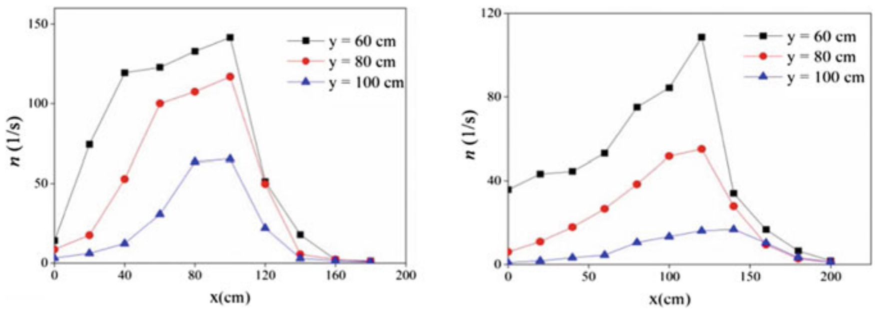

(a) $\beta = 48°, f = 0.9$ (b) $\beta = 48°, f = 3.2$

Fig. 6.16 Streamwise distribution patterns of the number frequency of water droplets n

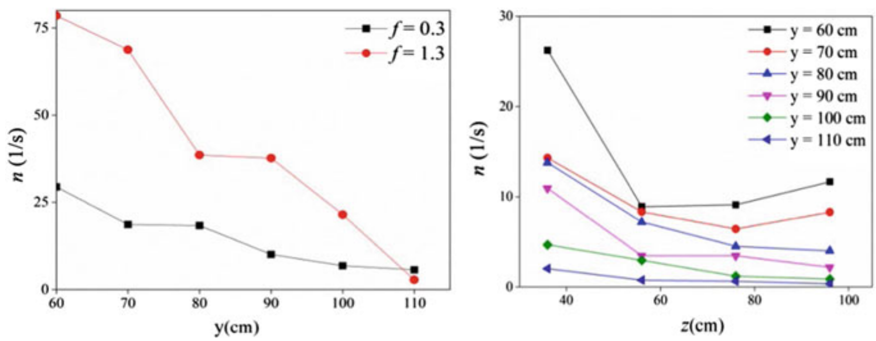

(a) $\beta = 90°$ (b) $\beta = 77°, f = 0.3$

Fig. 6.17 Transverse and vertical distribution patterns of n

was an insignificant change in $\overline{d}$ in both the transverse and streamwise cross-sections (Fig. 6.18).

In the experiment, the droplet velocity v was found to range from 0 to 15 m/s. There was a relatively high probability of v values of 0–3 m/s at the same measuring point (Fig. 6.19). $\overline{v}$ first increased and then decreased along the streamwise direction on various cross-sections and had an extreme value $\overline{v}_{\max}$. There was a certain distance between the location of $\overline{v}_{\max}$ and the collision point. In addition, the location of $\overline{v}_{\max}$ basically coincided with that of the extreme value of $\overline{d}$ ($\overline{d}_{\max}$) (Fig. 6.20). Moreover, there were similar patterns of variation in $\overline{v}$ and $\overline{d}$. The measured $\overline{d}$ of the water droplets that moved at a relatively high $\overline{v}$ was relatively large, and vice versa. This occurs because a relatively small water droplet is relatively significantly affected by drag and buoyancy and consequently moves relatively slowly. Thus, water droplets with a relatively large $\overline{d}$ moved at a relatively high $\overline{v}$, and water droplets with a

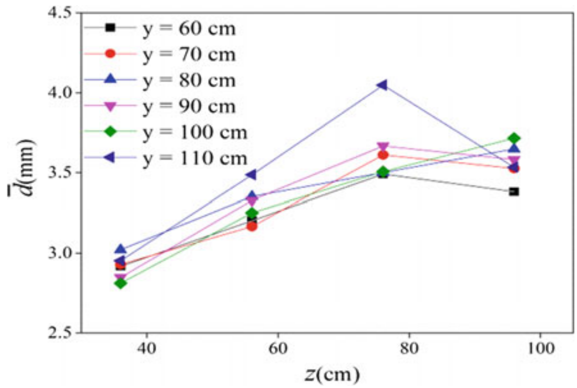

Fig. 6.18 Variations in the mean droplet diameter $\overline{d}$ in various cross-sections along the vertical direction

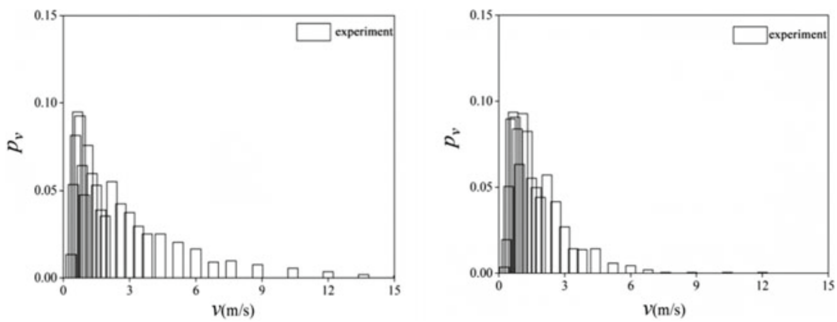

(a) $\beta = 48°, f = 0.9$, z = 96 cm, y = 60 cm, x = 60

(b) $\beta = 90°, f = 3.2$, z = 96 cm, y = 70 cm, x= $x_{I\max}$

Fig. 6.19 Probability distributions of the droplet velocity v at a given measuring point

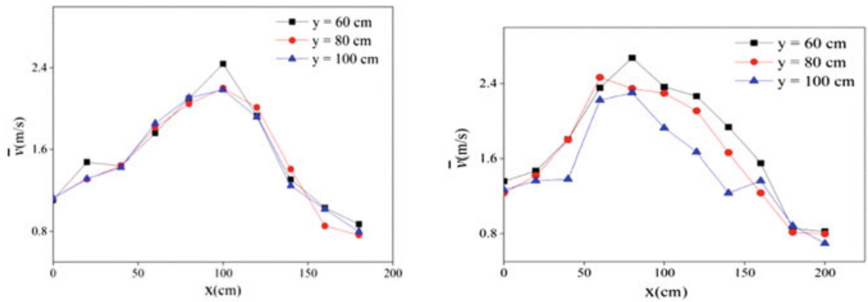

(a) $\beta = 48°, f = 0.9$ (b) $\beta = 90°, f = 1.3$

Fig. 6.20 Streamwise distribution patterns of the mean droplet velocity $\bar{v}$

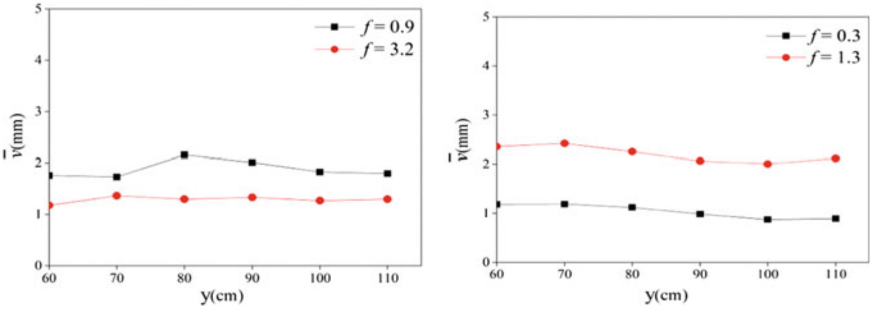

(a) $\beta = 48°$ (b) $\beta = 90°$

Fig. 6.21 Transverse distribution patterns of the mean droplet velocity $\bar{v}$

relatively small $\bar{d}$ moved at a relatively low $\bar{v}$, i.e., $\bar{v}$ was closely related to $\bar{d}$. $\bar{v}$ fluctuated to an insignificant extent along the transverse direction (Fig. 6.21). This pattern of variation was consistent with that in $\bar{d}$. This suggests that the patterns of variation in $\bar{v}$ and $\bar{d}$ were consistent in both the transverse and streamwise directions.

There were no significant changes in $\bar{v}$ along the vertical direction. As the vertical distance increased, $\bar{v}$ first increased and then decreased slightly. This was similar to the variation in $\bar{d}$ (Fig. 6.22). The similar variations in $\bar{v}$ and $\bar{d}$ suggest that the variations in $\bar{v}$ and $\bar{d}$ were similar in each spatial direction.

Figure 6.23 shows the relationship between the experimentally measured droplet diameter and velocity. In Fig. 6.23, the green curve shows the predicted values given by Clift et al. (2005), whose distribution trend is similar to that of the experimental results. However, Clift et al.'s (2005) values differ relatively significantly from the experimental values. The following droplet velocity–diameter relationship was established based on experimental measurements:

$$v = 9.5[1 - \exp(-0.4d)] \tag{6.6}$$

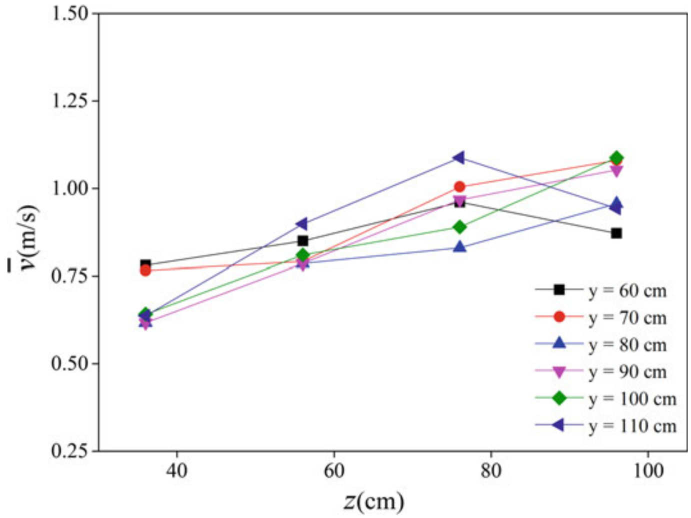

Fig. 6.22 Vertical distributions of the mean droplet velocity $\overline{v}$

Fig. 6.23 Experimental droplet velocity–diameter relationship

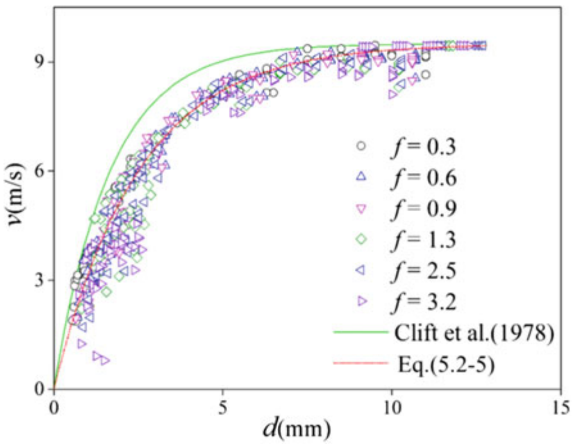

6.3.2 Effects of the Flow-Rate Ratio on the Characteristics of the Water Droplets Formed by a Jet Collision

Figure 6.24 shows the spallation of water droplets due to a two-jet collision in air. The flow-rate ratio had a significant impact on the results of the collision. When the flow rate of the upper jet was significantly lower than that of the lower jet, the postcollision mainstream moved basically along the original motion trajectory of the lower jet. In addition, under these conditions, most of the water droplets were formed from the spallation of the upper jet, and the water droplets splashed over a relatively

Fig. 6.24 Water droplets formed from spallation of jets as a result of collision in air

large area. When the flow rate of the upper jet was significantly higher than that of the lower jet, the postcollision mainstream moved basically along the original motion trajectory of the upper jet. Under these conditions, most of the water droplets were formed from the spallation of the lower jet, and the water droplets splashed over a relatively small area.

Moreover, the mean diameter $\overline{d}$ and mean velocity $\overline{v}$ of the water droplets were affected by the flow-rate ratio f. Specifically, $\overline{d}$ and $\overline{v}$ first increased and then decreased as f increased. $\overline{d}$ and $\overline{v}$ reached their respective maximum values when f was approximately 1 (Fig. 6.25).

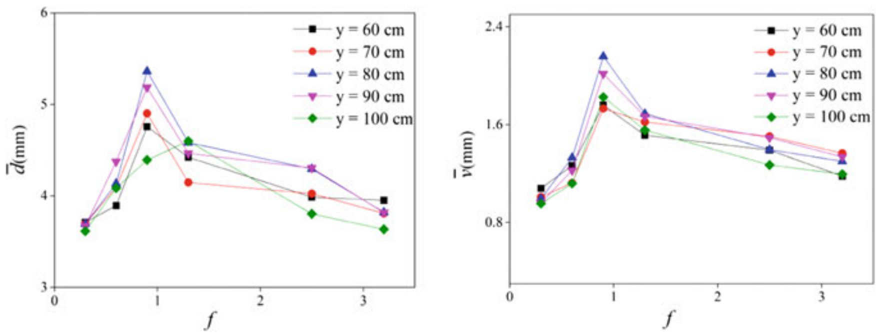

Fig. 6.25 Effects of the flow-rate ratio f on the mean diameter $\overline{d}$ and mean velocity $\overline{v}$ of water droplets (impingement angle $\beta = 48°$)

6.3.3 Spallation Area of Jets After Collision in Air

Collision in air between two jets increases the water droplet spallation area. Figure 6.26 shows the generalized characteristics of a collision in air between two jet nappes. V_1, θ_1, and q_1 are the flow velocity, angle of depression, and unit-width flow of the upper surface-outlet nappe when exiting from the bucket, respectively. V_2, θ_2, and q_2 are the flow velocity, trajectory angle, and unit-width flow of the deep-outlet nappe when exiting from the bucket, respectively. The two nappes converge at the point M. V_{1M} and β_1 are the flow velocity of the surface-outlet nappe and the angle between the surface-outlet nappe and the streamwise direction at the point M, respectively. V_{2M} and β_2 are the flow velocity of the lower deep-outlet nappe and the angle between the lower deep-outlet nappe and the streamwise direction at the point M, respectively. V_M, β_M, α_1, and α_2 are the takeoff flow velocity of the postcollision mixed nappe, the angle between the mixed nappe and the streamwise direction, the angle between the trajectory of the inner edge of the mixed nappe and the vertical direction (z-axis), and the angle between the trajectory of the outer edge of the mixed nappe and the streamwise direction (x-axis), respectively.

$$\tan \beta_M = \frac{q_1 \sin \beta_1 - q_2 \sin \beta_2}{q_1 \cos \beta_1 + q_2 \cos \beta_2} \tag{6.7}$$

$$V_M = \frac{V_{1M}(q_1 \cos \beta_1 + q_2 \cos \beta_2)}{q_M \cos \beta_M} \tag{6.8}$$

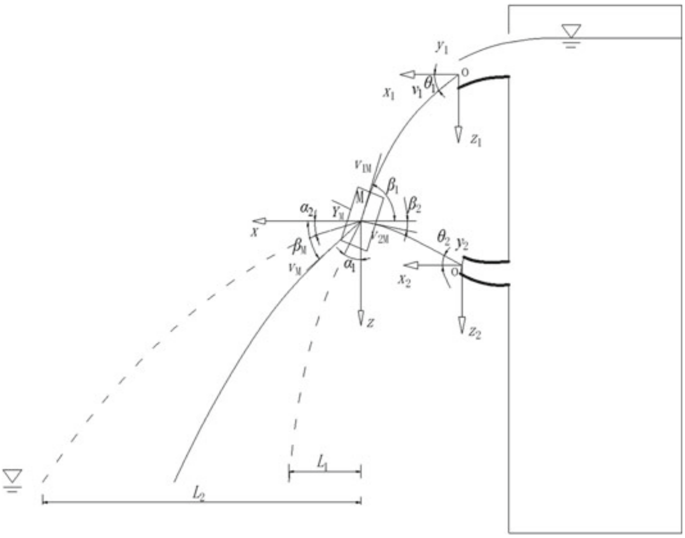

Fig. 6.26 Schematic diagram of a collision in air between deep- and surface-outlet nappes

In addition, the precollision values of V_{1M}, β_1, and β_2 must be determined. Thus, the parabolic trajectories of the surface- and deep-outlet nappes must be understood. The spatial location of the collision point M can be determined by ascertaining the trajectory of the inner edge of the surface outlet and the trajectory of the outer edge of the deep outlet. On this basis, V_{1M}, β_1, and β_2 can be calculated.

Figure 6.27 compares the measured and calculated locations of the maximum rainfall intensity $I_{\max}$. The measured locations of $I_{\max}$ are basically on the theoretical parabolas, with an error within 5%.

Next, the postcollision trajectories of the inner and outer edges of the mixed flow are discussed. First, the trajectory of the inner edge is discussed. Projectile motion was achieved at various angles with a velocity of V_M and the location of the collision point M as the origin of the coordinates. The previous analysis demonstrated that the shape of the trajectory of the inner edge of the nappe formed after collision between two jets is similar to that of a parabola and that the postcollision velocity can be calculated. The angles between the initial velocity and the streamwise and vertical directions were derived from each parabolic trajectory with a known velocity. The errors between each parabolic trajectory and the measured locations were basically within 5%. This suggests that the trajectories of the inner edge determined through theoretical analysis combined with experimental measurements are in good agreement with the measured values (Fig. 6.28).

α_1 was relatively significantly affected by the flow-rate ratio f and impingement angle β. If f remained unchanged, an increase in β resulted in an increase in α_1; if β remained unchanged, an increase in f resulted in an increase in α_1 (Fig. 6.29).

The effects of f and β on α_1 can be represented by the following equation:

$$\alpha_1 = 16\mathrm{e}^{(f \times \sin^2 \beta)} \tag{6.9}$$

where f ranges from 0.3 to 3.2 and β ranges from 48° to 90°.

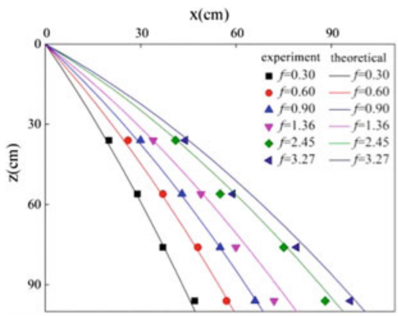

(a) $\beta = 48°$

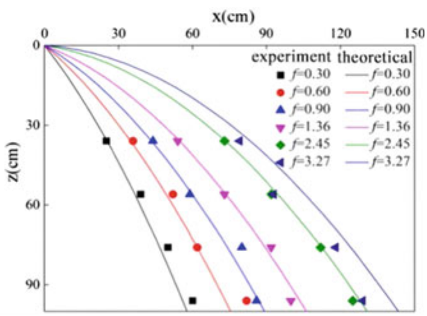

(b) $\beta = 77°$

Fig. 6.27 Comparison of measured and calculated locations of maximum rainfall intensity $I_{\max}$

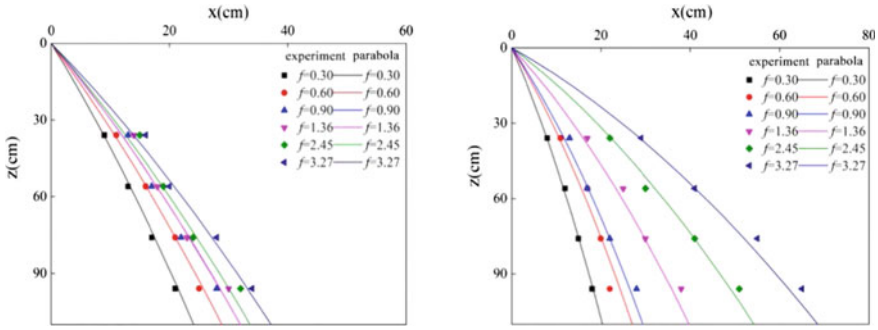

(a) $\beta = 48°$ (b) $\beta = 77°$

Fig. 6.28 Comparison of the measured and calculated trajectories of the inner edge of the nappe

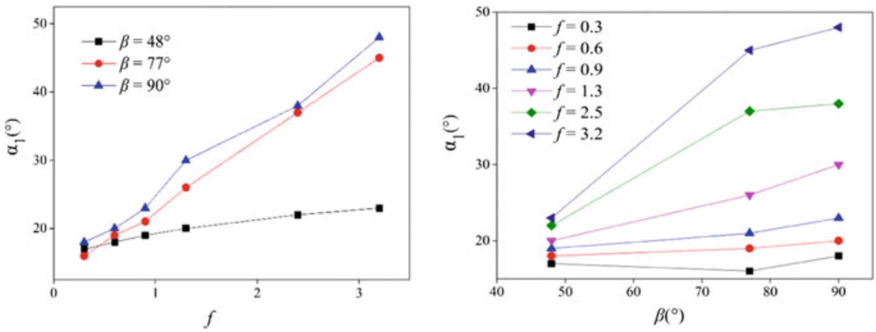

(a) Effects of f on α_1 (b) Effects of β on α_1

Fig. 6.29 Effects of the flow-rate ratio f and impingement angle β on α_1

Now, the trajectory of the outer edge is discussed. Similar to the trajectory of the inner edge, α_2 can be derived. Figure 6.30 compares the calculated and measured parabolic trajectories. As demonstrated in Fig. 6.30, there is a good agreement between the calculated and measured parabolic trajectories.

The variables f, β, and α_2 satisfy the relationship below:

$$\alpha_1 = 21 \times \sin\frac{\beta}{2} \times \ln(f) + 75.5 \times \tan\frac{\beta}{2} + 28.5 \tag{6.10}$$

where f ranges from 0.3 to 3.2 and β ranges from 48° to 90°.

The experimental results show that rainfall intensity I followed a Gaussian distribution in the streamwise direction and that I was relatively significantly affected by f and β. The following equation for the streamwise distribution of I was derived from the experimental results:

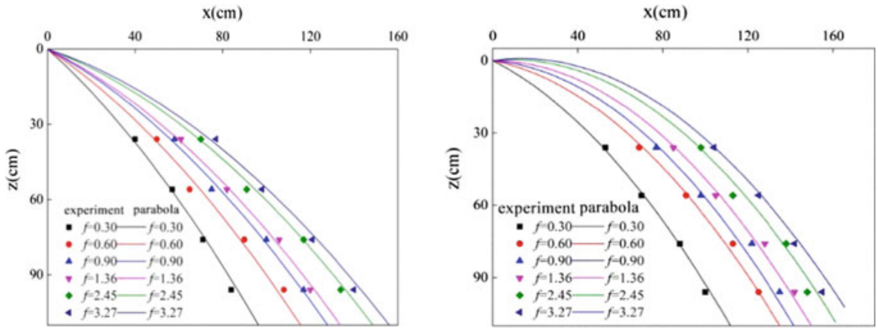

(a) $\beta = 48°$ (b) $\beta = 77°$

Fig. 6.30 Comparison of the measured and calculated trajectories of the outer edge of the nappe

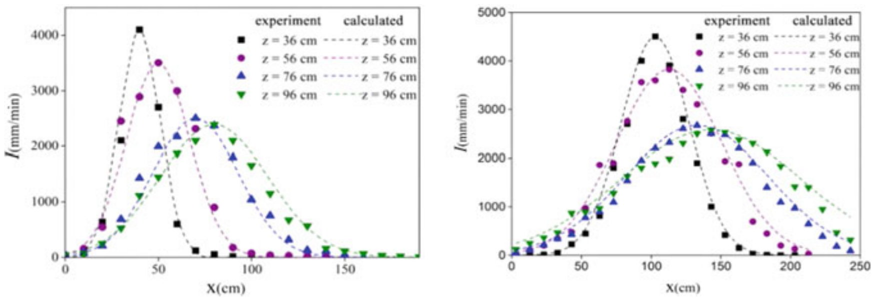

(a) $\beta = 77°, f = 0.9$ (b) $\beta = 90°, f = 3.2$

Fig. 6.31 Comparison of measured and calculated streamwise distributions of the rainfall intensity *I*

$$I = I_{max} \times e^{(-a\times(\frac{x-x_{max}}{z})^2)} \tag{6.11}$$

$$a = 10e^{(-1.8\times f)} + 20.5 - 20\tan\frac{\beta}{2} \tag{6.12}$$

where $I_{\max}$ is the maximum rainfall intensity measured under each set of conditions. As demonstrated in Fig. 6.31, the Gaussian distribution curves calculated using Eq. (6.11) are in good agreement with the measured values.

6.4 Water Splash by Plunging Jets

The splashing of downstream water caused by a plunging jet nappe is the largest source of atomization. Currently, when its characteristics are studied, the splashing of water caused by a plunging nappe is mainly divided into three stages of impact, splashing, and flow (Beltaos 1976; Sanjay and Das 2017a, b). In this section, the formation of water droplets from the splashing of water caused by a plunging jet as well as the movement of the water droplets after breaking away from the water are studied through mesoscale analysis of their motion characteristics. In addition, the effects of various jet parameters on splashing (the initial projection velocity v_p, splashing angle β_w, size (i.e., diameter d), and impact-point distance L_w of splashed water droplets) are investigated.

6.4.1 *Characteristics of the Water Droplets Splashed by a Jet*

The water droplets formed from the splashing of water by a plunging jet move in random directions. This section primarily analyzes several parameters of splashed water droplets, namely, β_w, d, and L.

First, β_w is analyzed. β_w under various experimental conditions was first calculated and then subjected to a gamma distribution test. Table 6.5 summarizes the results. The test results show that β_w followed a gamma distribution and that the jet-flow angle α_j of the jet was a main factor affecting β_w (Fig. 6.32).

Table 6.5 Gamma distribution test results for the splashing angle β_w

No.	Jet diameter D (cm)	Jet-flow angle α_j (°)	Jet-flow velocity U (m/s)	Calculated values of parameters			Probability (p-value)
				Alpha	Beta	Gamma	
1	0.8	30	8.37	1.76	27.94	1.89	0.915
2			11.32	1.51	26.53	2.96	0.985
3		60	8.37	5.00	15.51	17.48	0.960
4			11.97	21.06	8.47	118.52	0.985
5		90	8.64	5.83	15.73	5.19	0.960
6			11.97	25.62	9.57	147.15	0.527
7	1.6	30	4.09	1.83	33.45	11.32	0.269
8			5.40	1.53	28.40	4.54	0.684
9		60	4.40	4.48	15.20	7.72	0.997
10			6.27	4.74	12.33	−1.00	0.985
11		90	4.72	10.67	14.52	61.61	0.527
12			6.40	13.49	13.05	82.42	0.779

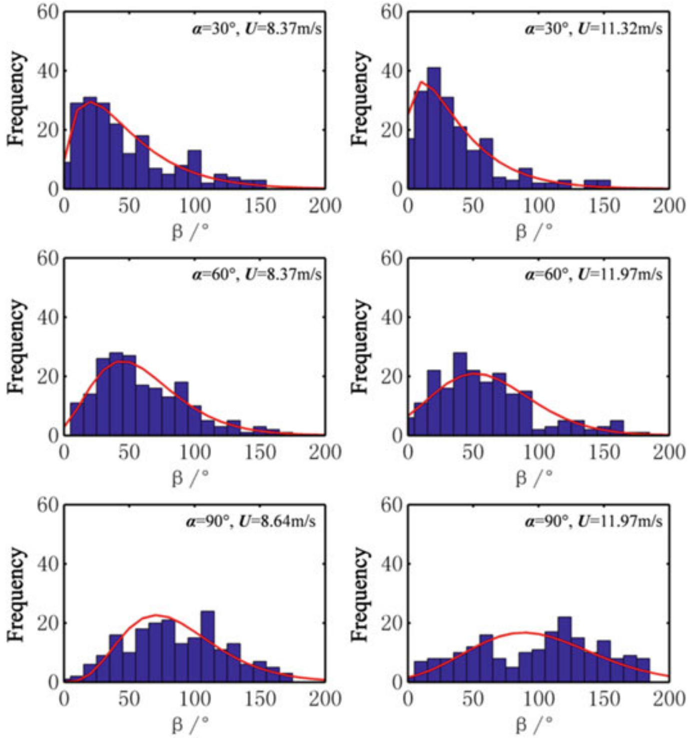

Fig. 6.32 Probability distributions of the splashing angle β_w when $D = 0.8$ cm

Second, the diameter of the splashed water droplets d is analyzed. d was statistically calculated and subjected to a gamma distribution test. Table 6.6 summarizes the results. The test results show that d basically followed a gamma distribution, though with a lower goodness of fit than that of β_w. This can also be observed in Fig. 6.33.

Table 6.6 Gamma distribution test results for the splashed water droplet diameter d under various conditions

No.	Jet diameter D (cm)	Jet-flow angle α_j (°)	Jet-flow velocity U (m/s)	Calculated values of parameters			Probability (p-value)
				Alpha	Beta	Gamma	
7	1.6	30	4.09	2.68	0.48	−0.54	0.081
8			5.40	3.38	0.55	−0.74	0.312
9		60	4.40	41.98	0.06	1.18	0.248
10			6.27	8.83	0.12	−0.14	0.312
11		90	4.72	13.91	0.08	0.06	0.061
12			6.40	3.05	0.20	−0.55	0.104

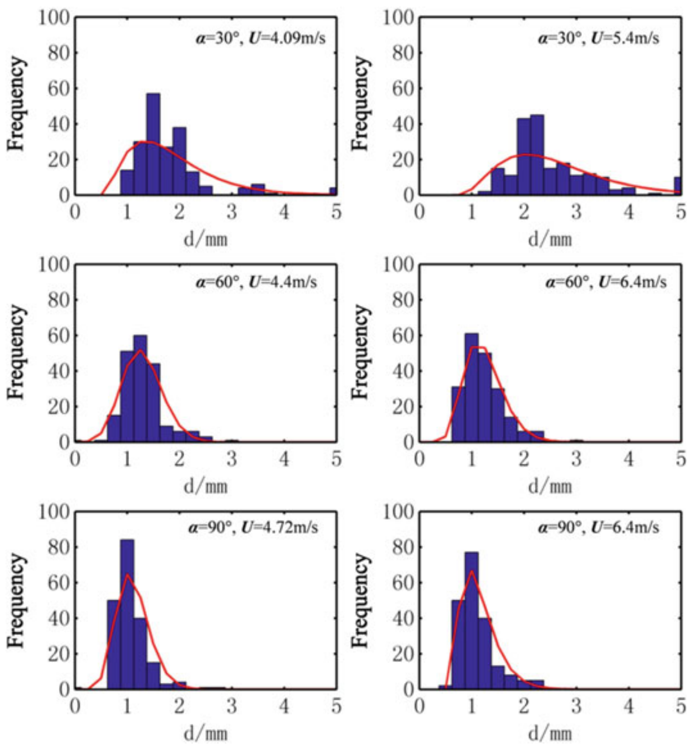

Fig. 6.33 Probability distributions of the splashed water droplet diameter d when $D = 1.6$ cm

Finally, the impact-point distance of the splashed water droplets, L, is analyzed. Table 6.7 and Fig. 6.34 both demonstrate that L similarly followed a gamma distribution.

Table 6.7 Gamma distribution test results for the impact-point distance of the splashed water droplets L_w

No.	Jet diameter D (cm)	Jet-flow angle α_j (°)	Jet-flow velocity U (m/s)	Calculated values of parameters			Probability (p-value)
				Alpha	Beta	Gamma	
7	1.6	30	4.09	19.41	0.02	0.22	0.779
8			5.40	16.78	0.01	0.12	0.997
9		60	4.40	2.61	0.02	0.02	0.985
10			6.27	2.39	0.02	0.02	0.985
11		90	4.72	3.53	0.04	0.16	0.310
12			6.40	4.00	0.04	0.15	0.449

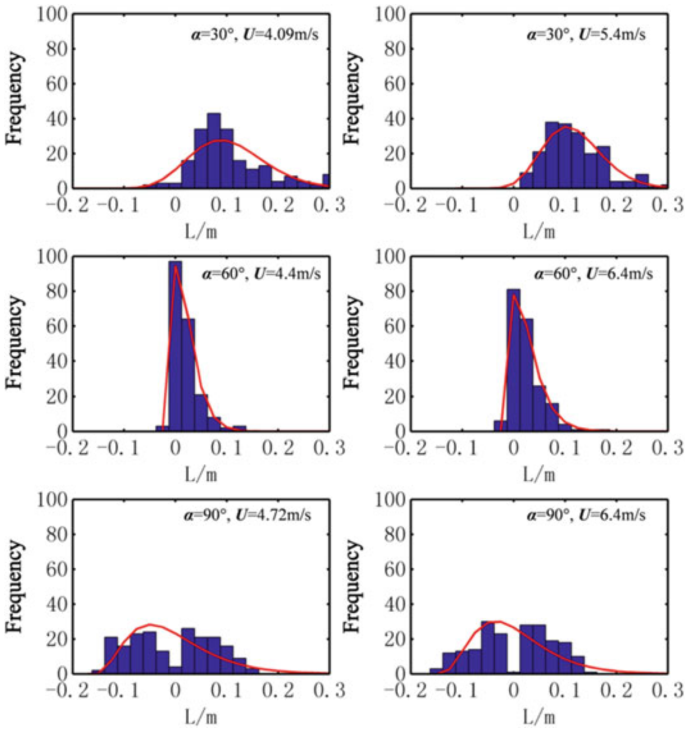

Fig. 6.34 Frequency distributions of the impact-point distance of the splashed water droplets, L, when $D = 1.6$ cm

6.4.2 Motion Pattern of the Water Droplets Formed by the Splashing of Water with a High-Velocity Plunging Jet

The initial projection velocity v_p of the water droplets formed by the splashing of water with a plunging jet plays a vital role in atomization. Table 6.8 and Fig. 6.35 show the following. At similar plunging velocities, the mean and peak values of the resultant velocity v_r of the splashed water droplets were the highest when the jet-flow angle $\alpha_j = 30°$. In addition, the mean and peak values of v_r of the splashed water droplets were significantly higher when $\alpha_j = 30°$ than when $\alpha_j = 60°$ and 90°. There was no significant difference in the mean and peak values of the v_r of the splashed water droplets between when $\alpha_j = 60°$ and when $\alpha_j = 90°$.

The velocity of the splashed water droplets can be further quantitatively analyzed. The collision between two jets satisfies the following equations:

$$J_x = m_1(u'_x - u_x) \tag{6.13}$$

Table 6.8 Distributions of the characteristic values of the initial resultant velocity v_r of the splashed water droplets

No.	Plunging jet			Initial v_r of splashed water droplets (m/s)			
	Jet diameter D (cm)	Jet-flow angle α_j (°)	Jet-flow velocity U (m/s)	Maximum	Minimum	Mean	Peak
1	0.8	30	8.37	2.86	0.08	1.05	0.89
2			11.32	3.15	0.15	1.14	0.94
3		60	8.37	2.67	0.14	0.77	0.51
4			11.97	2.03	0.11	0.73	0.61
5		90	8.64	2.28	0.14	0.89	0.77
6			11.97	2.62	0.15	0.96	0.65
7	1.6	30	4.09	3.25	0.13	1.17	0.92
8			5.40	3.5	0.13	1.29	1.13
9		60	4.40	2.41	0.17	0.74	0.46
10			6.27	2.45	0.12	0.74	0.43
11		90	4.72	2.49	0.14	0.83	0.66
12			6.40	4.32	0.23	0.83	0.71

$$J_y = m_1(u'_y - u_y) \tag{6.14}$$

$$-J_x = m_2(v'_x - v_x) \tag{6.15}$$

$$-J_y = m_2(v'_y - v_y) \tag{6.16}$$

where J_x and J_y are the impulse components at the collision point in the horizontal and vertical directions, respectively, m_1 is the precollision mass of the upper jet, u_x and u_y are the precollision velocity components of the upper jet in the horizontal and vertical directions, respectively, m_2 is the precollision mass of the lower jet, v_x and v_y are the precollision velocity components of the lower jet in the horizontal and vertical directions, respectively, u_x' and u_y' are the postcollision generalized velocity components of the upper jet in the two-dimensional (2D) directions, and v_x' and v_y' are the postcollision generalized velocity components of the lower jet in the 2D directions.

In the vertical (y) direction, the differences between the velocities before and after the collision point as well as a recovery coefficient are introduced:

$$G_y = u_y - v_y \tag{6.17}$$

$$G'_y = u'_y - v'_y \tag{6.18}$$

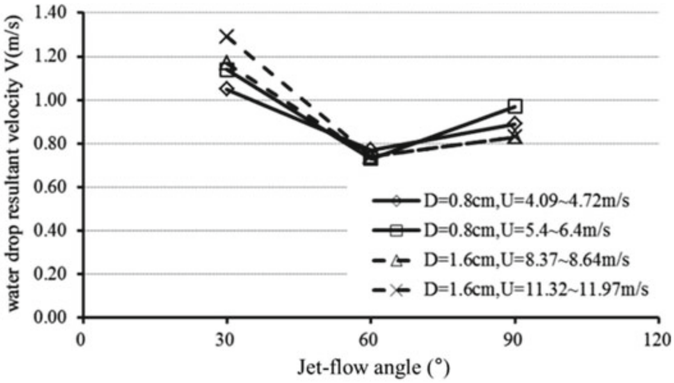

(a) Variation of the mean v_r of splashed water droplets

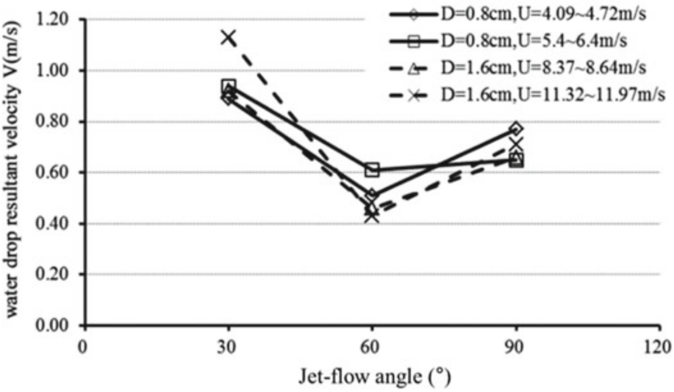

(b) Variation in the peak v_r of the splashed water droplets

Fig. 6.35 Distributions of the characteristic values of the resultant velocity v_r of the splashed water droplets

$$e = -\frac{G'_y}{G_y} \tag{6.19}$$

Thus

$$G'_y - G_y = u'_y - u_y - (v'_y - v_y) = \frac{m_1 + m_2}{m_1 m_2} J_y \tag{6.20}$$

The impulse J_y in the vertical direction is

$$J_y = -(1 + e)\frac{m_1 m_2}{m_1 + m_2} G_y \tag{6.21}$$

According to Coulomb's law of friction,

$$\frac{J_x}{J_y} = c \tag{6.22}$$

The velocity components after the collision point are

$$u_x' = u_x - f(1+e)(u_y - v_y)\frac{m_2}{m_1 + m_2} \tag{6.23}$$

$$v_y' = u_y' + e(u_y - v_y) \tag{6.24}$$

For the splashing of water caused by a plunging jet, the location of the water surface is used as the collision boundary, i.e., $u_x{}' = u_y{}' = 0$, and $v_x = v_y = 0$. Thus, we have

$$e = \frac{v_y'}{u_y} \tag{6.25}$$

$$u_x' = u_x - f(1+e)\frac{m_2}{m_1 + m_2}u_y \tag{6.26}$$

The mass m_2 of the free surface can be treated as infinite relative to the mass m_1 of the impacting jet, i.e., $m_2 >> m_1$. Thus, we have

$$u_x' = u_x - c(1+e)u_y \tag{6.27}$$

The jet-flow velocity U and jet-flow angle α_j are the factors that affect the recovery coefficient e for a free surface impacted by a jet, as shown in Fig. 6.36. As U and α_j increased, there was a gradual decrease in e. This suggests that there was a moderate decrease in the vertical velocity v_Y of the water droplets splashed by a high-velocity, large-angle jet upon impact of a free surface (a deformable boundary) after being reflected by the free surface. Sufficiently deep water is capable of absorbing more impact energy from a jet. Let d_m be the mean diameter d of the water droplets formed from the splashing of water by a plunging jet. Equation (6.28) shows the approximate relationship between α_j and ed_m/D. Figure 6.37 shows the relationships of e with U and α_j.

$$e(d_\mathrm{wm}/D) = 0.035 - 0.025\sin\alpha_\mathrm{j} \tag{6.28}$$

Figure 6.38 shows the relationship between the resistance coefficient c and the flow conditions during the splashing of water caused by a plunging jet. The experimental results show that c was affected primarily by α_j. As α_j increased, there was a significant decrease in c.

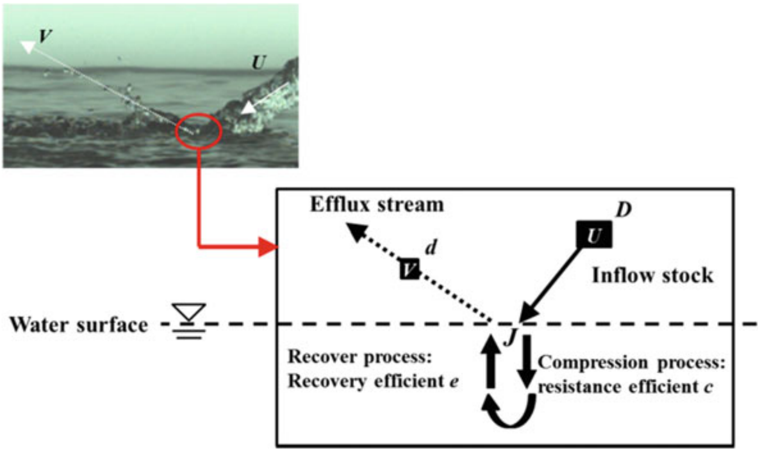

Fig. 6.36 Generalized diagram of the splashing of water droplets by a jet upon impact of a free surface

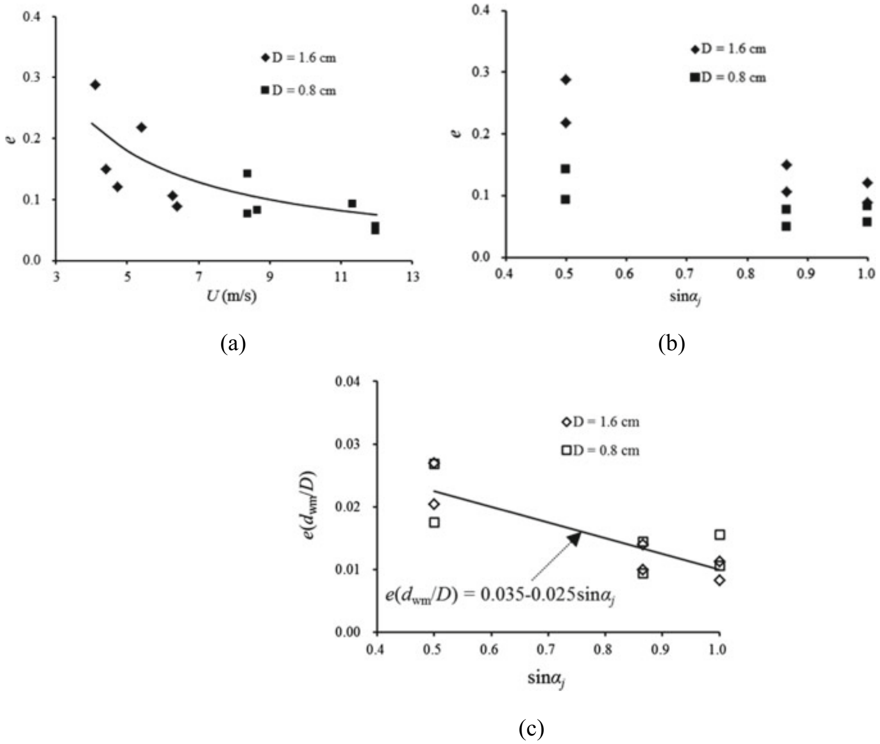

Fig. 6.37 Relationships of the recovery coefficient e with the jet-flow velocity U and jet-flow angle α_j

Fig. 6.38 Variation in the resistance coefficient *c*

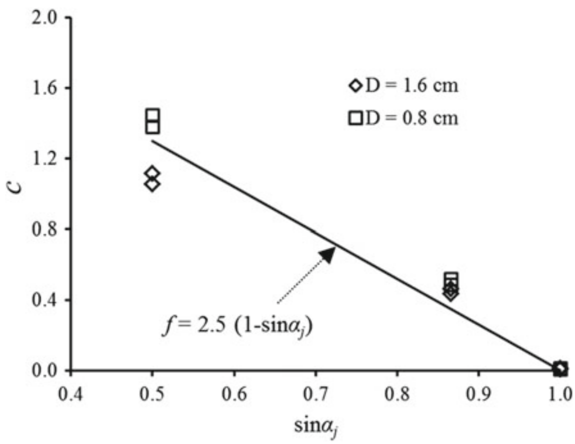

6.5 Discussion of the Scale Effect in Flood Discharge Atomization Model Tests for High-Head Dams

Model tests are one of the main approaches to predict FDA for dams. However, model test results often differ relatively significantly from prototype measurements. Thus, the scale effect is a prominent problem faced in FDA model tests.

6.5.1 *Similarity Criterion for FDA Model Tests*

An FDA model is designed based on the gravity similarity criterion. The variables of a prototype structure and its model satisfy the following relationship:

$$\frac{v_P^2}{g_{\mathrm{P}} L_P} = \frac{v_M^2}{g_{\mathrm{M}} L_M} \tag{6.29}$$

where v_P and v_M are the velocities of the prototype structure and the model, respectively, L_P and L_M are the lengths of the prototype structure and the model, respectively, and g is the gravitational acceleration.

The gravity similarity criterion treats gravity as the main acting force in the flow of a liquid. However, the surface tension of a liquid also has a relatively significant impact during the atomization of its flow. Thus, a relatively high flow velocity (e.g., >6 m/s) and a relatively large Weber number *We* (e.g., >500) are required for an FDA model test (Wu et al. 2011). However, except for a 1:1 scale, it is difficult to meet the gravity similarity criterion while also meeting the *We* similarity criterion in a model. In other words, the following equation cannot be satisfied:

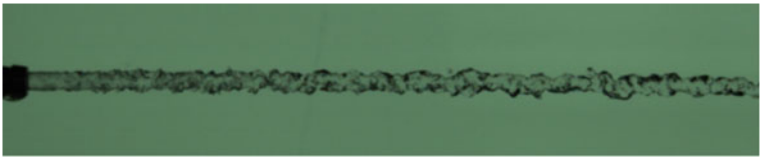

(a) $v_0 = 9.46$ m/s, $Re = 41{,}212$, $We = 5{,}413$

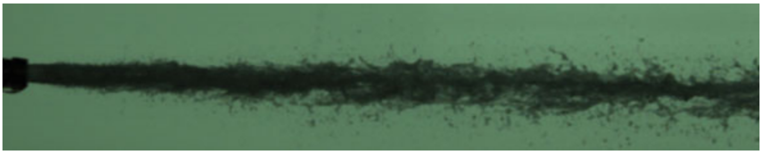

(b) $v_0 = 22.74$ m/s, $Re = 99{,}065$, and $We = 31{,}275$

Fig. 6.39 Comparison of the spallation forms of 4.5-mm jets at low- and high-velocities (v_0), respectively

$$\frac{\rho_P l_P V_P^2}{\sigma_\mathrm{p}} = \frac{\rho_M l_M V_M^2}{\sigma_\mathrm{M}} \tag{6.30}$$

where ρ is the density, l is the characteristic length of the flow, V is the velocity of the flow, and σ is the surface tension coefficient. Thus, an FDA model test does not strictly follow the similarity laws.

6.5.2 Scale Effect in FDA Model Tests

Figure 6.39 shows the spallation of jets at flow velocities of approximately 10 and 20 m/s, respectively. Almost no water droplets were spalled from the jet at a relatively low flow velocity within the limited window. In comparison, the jet at a relatively high flow velocity spalled significantly, resulting in the formation of a large number of splashed water droplets. In a model test, even one with a large-scale model, the jet flow velocity is generally lower than 10 m/s. Thus, it is difficult to simulate the spallation of a flow.

In regard to the selection of a scale for an FDA model test, a jet flow velocity higher than 6 m/s and a *We* greater than 500 are generally required. However, the experimental observations were as follows. The set of experimental conditions consisting of a *D* of 4.5 mm, a *We* of 5413 and a jet flow velocity of 9.46 m/s as well as that consisting of a *D* of 5.5 mm, a *We* of 7440 and a jet flow velocity of 9.92 m/s completely meet the requirements that the *We* value be greater than 500 and the jet flow velocity be higher than 6 m/s. Nevertheless, almost no water droplets were spalled from the 4.5-mm jet within the window. While an extremely small number of water droplets were present within the window for the 5.5-mm jet, this jet was far from significantly spalled.

In fact, the experimental observations found the following. (1) When D remained unchanged, as the jet flow velocity increased, there was a gradual increase in the extent of spallation of the jet, a gradual decrease in the length of the stable section of the jet after discharge from the outlet, and a continuous increase in the α_s of the water droplets. In addition, the smallest water droplets spalled from a high-velocity jet were even smaller than those spalled from a low-velocity jet in terms of d. (2) At a relatively low jet flow velocity, the 4.5-mm jet spalled to a lesser extent than the 5.5-mm jet and remained relatively highly stable. In addition, at a relatively low jet flow velocity, the 4.5-mm jet did not significantly disperse into water droplets. At a relatively high jet flow velocity, the mainstream of the 4.5-mm jet broke up violently, resulting in the formation of a large number of water droplets of varying d values and high α_s values. At a relatively high jet flow velocity, the 4.5-mm jet spalled to a notably greater extent than the 5.5-mm jet. (3) At a relatively low jet flow velocity, water droplets were mainly formed as a result of the surface turbulence of a jet. At a relatively high jet flow velocity, apart from the water droplets formed as a result of turbulence, large water masses broke away from a jet. These water masses further broke up into small water droplets as a result of air drag (Fig. 6.2). Thus, the spallation of a high-velocity jet into water droplets differs from that of a low-velocity jet.

It is difficult to use a reduced-scale model to reasonably simulate the spallation of a jet. However, Sect. 6.4 of this chapter shows that a reduced-scale model is capable of more reasonably and accurately simulating the splashing of water caused by an impacting jet. In addition, the drift of mist in air is not primarily controlled by gravity. Thus, an FDA model test is capable of relatively satisfactorily simulating the splashing of water caused by an impacting jet but incapable of effectively simulating the spallation of a jet in air and the drift of mist.

6.6 Conclusions

The following summarizes the main conclusions derived from the analysis in this chapter:

1. The extent of the spallation of a high-velocity jet increases as the jet flow velocity increases. In addition, the spallation patterns of high- and low-velocity jets are different.
2. The splashing angle β_w and diameter d of the water droplets formed from the splashing of water caused by a high-velocity plunging flow both follow a gamma distribution.
3. Two-jet collision in air significantly increases the FDA intensity and is significantly affected by the flow-rate ratio f and impingement angle β.
4. An FDA model test is capable of relatively satisfactorily simulating the splashing of water caused by a plunging jet but incapable of effectively simulating the spallation of a jet in air and the drift of mist.

References

Beltaos, S. (1976). Oblique impingement of plane turbulent jets. *Journal of the Hydraulics Division, 102*(9), 1177–1192.

Choo, Y., & Kang, B. (2007). The effect of jet velocity profile on the characteristics of thickness and velocity of the liquid sheet formed by two impinging jets. *Physics of Fluids, 19*(11), 112101.

Clift, R., Grace, J. R., & Weber, M. E. (2005). *Bubbles, drops, and particles*. Courier Corporation.

Hoyt, J. W., & Taylor, J. (1977). Waves on water jets. *Journal of Fluid Mechanics, 83*(1), 119–127.

Lian, J., Liu, F., & Zhang, H. (2006). Numerical simulation of atomization due to flood discharges of hydropower stations.

Lian, J., Li, C., Liu, F., & Wu, S. (2014). A prediction method of flood discharge atomization for high dams. *Journal of Hydraulic Research, 52*(2), 274–282.

Liang, Z. (1992). A computation model for atomization flow. *Journal of Hydrodynamics, 3*.

Liu, H., Sun, S., Liu, Z., & Wang, X.-S. (2005). Atomization prediction based on artificial neural networks for flood releasing of high dams. *Journal of Hydraulic Engineering Division of the American Society of Civil Engineers, 36,* 1241–1245.

Reitz, R., & Bracco, F. (1982). Mechanism of atomization of a liquid jet. *The Physics of Fluids, 25*(10), 1730–1742.

Sanjay, V., & Das, A. K. (2017a). Formation of liquid chain by collision of two laminar jets. *Physics of Fluids, 29*(11), 112101.

Sanjay, V., & Das, A. K. (2017b). On air entrainment in a water pool by impingement of a jet. *AIChE Journal, 63*(11), 5169–5181.

Sun, S. (2009). Summary of research on flood discharge and energy dissipation of high dams in China. *Journal of China Institute of Water Resources and Hydropower Research, 2*.

Sun, X.-F., & Liu, S.-H. (2008). Investigation on the motion of splash droplets in atomized flow. *Journal of Hydrodynamics (Ser. A), 1*.

Wang, S.-Y., Chen, D., & Hou, D.-M. (2013). Experimental research on the rainfall intensity in the source area of flood discharge atomization. *Journal of Yangtze River Scientific Research Institute, 8,* 19.

Wu, S., Wu, X., Zhou, H., Chen, H., Sha, H., & Zhou, J. (2011). Analysis and application of the scale effect of flood discharge atomization model. *Science China Technological Sciences, 54*(1), 64–71.

Yuan, H., Xu, W., Li, R., Feng, Y., & Hao, Y. (2018). Spatial distribution characteristics of rainfall for two-jet collisions in air. *Water, 10*(11), 1600.